

Direct Numerical Simulation of a Hypersonic Turbulent Boundary Layer on a Large Domain

Stephan Priebe*, M. Pino Martín†

The direct numerical simulation (DNS) of a spatially-developing hypersonic turbulent boundary layer is presented. The freestream Mach number is $M_\infty = 7.2$. The simulation is performed on a large computational domain resulting in a variation of Reynolds number based on momentum thickness from a value of $Re_\theta = 1650$ at the inlet of the domain to $Re_\theta = 3300$ at the outlet. A large rescaling length is used in the prescription of the inflow boundary condition to minimize spurious numerical correlation between the inflow and recycling plane. The evolution of boundary layer parameters and basic statistics with streamwise distance through the computational box is investigated. An effect of the wall temperature condition in the DNS (cold wall) on the behavior of the boundary layer is observed.

I. Introduction

There are few studies of hypersonic flows at Mach number greater than 5 and few involve the measurement of mean and fluctuating quantities in the flow field. As pointed out in the review article by Roy and Blottner,¹ a need exists for new experiments and simulations which give information on mean and fluctuating quantities in the flow field to improve our physical understanding of hypersonic flows and to improve turbulence models and their predictive capabilities.

Particle image velocimetry (PIV) of high-speed flows is now becoming feasible. Examples of applications of PIV to high-speed flows include Schrijer, Scarano and van Oudheusden;² Sahoo, Ringuette and Smits;³ and Schreyer, Sahoo and Smits.⁴

In our first series of papers,⁵⁻⁸ we perform DNS of supersonic and hypersonic turbulent boundary layers to assess and generalize commonly used scalings in the presence of strong wall cooling, high enthalpy and high Mach number flow conditions. In this paper, we present initial results for the DNS of a spatially-developing hypersonic turbulent boundary layer at Mach 7.2 on a large domain. We study the evolution of the rescaled inflow boundary layer and assess the quality of the data downstream.

II. Numerical method and computational setup

The full three-dimensional unsteady Navier–Stokes equations in conservation form are solved for a perfect gas. The equations are expressed in dimensionless form. The usual constitutive relations for a Newtonian fluid are used: the viscous stress tensor is linearly related to the rate of strain tensor, and the heat flux vector is linearly related to the gradient of temperature through Fourier’s law of heat conduction. The coefficient of viscosity μ is computed from Keyes⁹ law, which is given by $\mu_K = 1.488 \times 10^{-6} \sqrt{T} / (1 + (122.1/T)10^{-5/T})$.

Figure 1(a) plots the viscosity as given by Keyes law and the usual Sutherland’s law over the range of temperatures in the present simulation, in which the freestream temperature is relatively low ($T_\infty = 62.9K$) and the wall temperature is set to $T_w = 340K$. The relative error between Keyes and Sutherland’s law $\Delta\epsilon_\mu = (\mu_K - \mu_S)/\mu_S$ is plotted in figure 1(b). The two viscosity laws agree for temperatures $T > 150K$, for which the relative error is $\Delta\epsilon_\mu < 1\%$. At lower temperatures, the viscosity laws diverge. At these temperatures, Keyes law is more accurate and its use is recommended over Sutherland’s law (see Roy and Blottner¹). Since temperatures as low as $60K$ are encountered in the present simulation, we use Keyes law.

*Graduate Student, Department of Mechanical and Aerospace Engineering, Princeton University. Visiting Graduate Student, Department of Aerospace Engineering, University of Maryland, College Park.

†Associate Professor, Department of Aerospace Engineering, University of Maryland, College Park.

The governing equations are solved using a fourth-order weighted essentially non-oscillatory (WENO) scheme to discretize the inviscid fluxes. Compared with the original finite-difference WENO scheme introduced by Jiang and Shu,¹⁰ which is too dissipative for the accurate computation of compressible flows, the present scheme is modified: the modification concerns the linear part of the scheme, that is, the scheme in smooth flow regions where a set of optimal WENO weights is engaged. The modification consists in adding a fully-downwinded candidate stencil, which gives a symmetric collection of candidate stencils, and in optimizing the WENO weights to maximize bandwidth-resolving efficiency.¹¹ The resulting symmetric bandwidth-optimized WENO scheme has been extensively validated for the computation of compressible turbulence and high-speed turbulent boundary layer flows (see Martín et al.,¹¹ Martín,⁵ and Duan et al.⁶).

For the discretization of the viscous fluxes, standard fourth-order central differences are used, and time integration is performed by means of a third-order low-storage Runge–Kutta method.¹²

The streamwise, spanwise and wall normal coordinates are denoted by x , y and z , respectively. The computational box for the DNS measures $L_x/\delta_{ref} = 27.0$ in the streamwise direction, $L_y/\delta_{ref} = 10.0$ in the spanwise direction, and $L_z/\delta_{ref} = 14.2$ in the wall normal direction, where $\delta_{ref} = 5mm$ is the reference length which is approximately equal to the boundary layer thickness at the outlet of the computational domain (see § III below). The grid has $N_x \times N_y \times N_z = 840 \times 768 \times 150$ points (total of approx. 96.8 million points). The grid is uniformly spaced in the streamwise and spanwise directions, whereas it is stretched in the wall normal direction following a geometric stretching function. The grid resolution at the inlet of the computational domain is: $\Delta x^+ = 7.5$; $\Delta y^+ = 3.0$; the first grid point away from the wall is located at $z_2^+ = 0.3$, there are 24 points within $z^+ < 10$, and the grid spacing at the edge of the boundary layer is $\Delta z/\delta_{99} = 0.04$. A grid resolution study has been performed by running temporal DNSs at the same flow conditions as the present simulation and with several grid resolutions. The results are found to be grid-converged at the resolution used in the present simulation.

The freestream conditions in the present DNS are as follows: the velocity is $U_\infty = 1146.1m/s$, the density is $\rho_\infty = 7.43 \times 10^{-2}kgm^{-3}$, the temperature is $T_\infty = 62.9K$, and the Mach number is $M_\infty = 7.21$.

Concerning the boundary conditions for the simulation, a no-slip isothermal boundary condition is used at the wall, where the temperature is set to $T_w = 340K$. Supersonic exit boundary conditions are used at the top and outlet boundaries. Given the high Mach number of the flow and the resulting proximity of the sonic line to the wall, no significant spurious effects are expected to travel from the outlet back into the domain. Consequently, it is not required to prescribe a sponge layer at the outlet of the domain. Periodicity is prescribed in the spanwise direction. The inflow boundary condition is prescribed by means of the recycling-rescaling technique developed by Xu and Martín.¹³ To minimize spurious numerical correlations and coupling between the inflow plane and the recycling plane, a large rescaling length is required. In the present simulation, the recycling plane is located at $x_{rec}/\delta_{ref} = 26.0$ downstream of the inflow plane.

III. Results

III.A. General flow structure

The general flow structure is shown in figures 2 and 3. Figure 2 shows two typical numerical Schlieren visualizations. Turbulent eddies of length scale $O(\delta)$ are visible in the outer region of the boundary layer. Large values of the numerical Schlieren index and hence of magnitude of density gradient are present at the interface between the irrotational freestream flow and the rotational boundary layer flow. In this high Mach number flow, the freestream just above the boundary layer contains disturbances that appear to be radiated from the boundary layer structures into the freestream. The visualizations also show the substantial growth of the boundary layer through the computational domain. It may be estimated visually that the boundary layer thickness approximately doubles from the inlet to the outlet of the domain.

Similar observations as from the numerical Schlieren visualizations can be made from figure 3, which shows the instantaneous three-dimensional structure of the flow. The isosurface of magnitude of density gradient shown reveals the structure of the bulges of length scale $O(\delta)$ in the outer region of the boundary layer. These structures grow substantially through the computational domain in the streamwise, spanwise and wall normal direction. The numerical Schlieren visualizations shown on the (x, z) -plane corresponding to the $y = L_y$ -boundary of the domain shows the radiation of disturbances from the boundary layer into the freestream. The disturbances are confined to the vicinity of the boundary layer. At the outlet of the computational domain, the disturbances appear to be confined to roughly $z/\delta_{ref} < 4$.

III.B. Boundary layer parameters and statistics

In this section, we analyze the evolution with streamwise distance of various boundary layer parameters and basic statistics. This analysis also serves to investigate the effect of the rescaling inflow boundary condition on the flow, and to assess what initial portion of the box is unphysical due to the rescaling and must be discarded.

Figure 4(a) shows the evolution of δ_{99} with streamwise distance, where δ_{99} is the thickness based on 99% of U_∞ . The boundary layer grows substantially through the computational domain: at the inlet, the thickness is $\delta_{99}/\delta_{ref} = 0.45$ ($\delta_{99} = 2.25mm$); at the outlet, the thickness is approximately $\delta_{99}/\delta_{ref} = 0.9$ ($\delta_{99} = 4.5mm$).

The growth of the boundary layer is also apparent from the evolution of the momentum thickness θ (shown in figure 4(b)) and from the evolution of the displacement thickness δ^* (shown in figure 4(c)). At the outlet, the momentum thickness is approximately $\theta/\delta_{ref} = 0.035$ ($\theta = 0.175mm$) and the displacement thickness is approximately $\delta^*/\delta_{ref} = 0.5$ ($\delta^* = 2.5mm$).

Figure 4(d) shows the evolution of the shape factor $H = \delta^*/\theta$. This quantity is not yet fully converged, but the following behavior appears to develop: the values of H observed near the outlet and inlet of the computational domain are approximately equal at $H = 14$. Downstream from the inlet, the value of H drops due to the lower local Reynolds number. Downstream of approximately $x/\delta_{ref} = 5$, the shape factor is seen to increase gradually with downstream distance as the Reynolds number of the flow increases. Based on these observations, it would appear that the first 5 – 10 δ_{ref} of the computational box are probably unphysical due to the rescaling and must be discarded, but better converged data is necessary to draw such a conclusion with confidence.

As can be seen from figure 5, the Reynolds number based on momentum thickness $Re_\theta = U_\infty\theta/\nu_\infty$ approximately doubles through the computational box, from a value of $Re_\theta = 1650$ at the inlet to a value of $Re_\theta = 3300$ at the outlet.

Figure 6(a) shows the evolution of the skin friction coefficient C_f with streamwise distance. The van Driest II prediction is shown for comparison (see van Driest¹⁴ and also Hopkins and Inouye¹⁵). The relative error between the VDII prediction and the DNS results is plotted in figure 6(b). At the inlet of the domain, the value of C_f is approximately 5% above the VDII prediction. With streamwise distance, the value of C_f falls below the VDII prediction and then recovers to pass above it again. Starting at approximately $x/\delta_{ref} = 13$, the value of C_f follows the trend of the prediction but is shifted to slightly larger values with an error that is approximately constant at a value of 5%. We attribute this shift to the wall-temperature condition in the DNS. The wall temperature is set to $T_w = 340K$, and the adiabatic recovery temperature is $T_r = T_\infty(1 + r(\gamma - 1)/2M_\infty^2) = 645K$ assuming a recovery factor of $r = 0.89$. The ratio of wall temperature to adiabatic recovery temperature is thus $T_w/T_r = 0.53$. Duan et al.⁶ have performed DNS studies to investigate the effect of varying wall temperature condition on the properties of super- and hypersonic boundary layers to assess the validity of commonly used scalings. Varying the wall temperature condition in a Mach 5 boundary layer, they find that the skin friction coefficient is generally well predicted by the VDII scaling across the range of wall temperature conditions. However, there are some slight departures from the prediction, and at the condition with $T_w/T_r = 0.5$, the value of C_f in their simulation lies approximately 5% above the VDII prediction. This is consistent with the departure from the VDII prediction observed in the present simulation, and we thus argue that this departure is a wall-temperature effect. In addition, we may conclude from figure 6 that the boundary layer, which is driven out of equilibrium by the rescaling procedure, recovers to an equilibrium state within approximately $x/\delta_{ref} = 13$ from the inlet. The initial portion of the box ($x/\delta_{ref} < 13$) is unphysical and must be discarded for the purpose of collecting flow statistics.

Figure 7 shows the van Driest transformed velocity u_{VD}^+ at different streamwise locations in the second half of the box. To obtain better statistical convergence, the profiles have been obtained over a streamwise window that measures $\Delta x/\delta_{ref} = 2$ and is centered at the stations given on the plot. The profiles show a short log law region where $u_{VD}^+ = (\log z^+)/\kappa + C$.

The usual value of $\kappa = 0.41$ fits the data but the additive constant is greater than the usual value of $C = 5.2$; a value of $C = 5.9$ fits the data. The slight increase in the additive constant C from a value of 5.2 to 5.9 is also a wall temperature effect. Duan et al.⁶ observe this effect in DNS at Mach 5 with varying wall temperature condition (see figure 5 in their paper). Furthermore, we have performed a grid convergence study which shows that the present data are grid converged and that for much finer grids this shift of the log law to $C = 5.9$ is present unchanged.

III.C. Spectra

In this section, we present spectra of pressure, streamwise velocity and streamwise mass flux which were obtained at the recycling station ($x_{rec}/\delta_{ref} = 26$) near the outlet of the domain.

Figure 8 shows the spectrum of wall pressure at the recycling station. The energy is broadband and centered approximately around the characteristic frequency of the boundary layer at $f\delta_{ref}/U_\infty = 1$ with a spectral peak at slightly higher frequency of approximately $f\delta_{ref}/U_\infty = 2$. There is no energy near the characteristic frequency of the rescaling.

Figure 9 shows the streamwise velocity and mass flux spectra at three different wall normal locations: (a) the location of the inner peak $z^+ = 15$; (b) the middle of the log layer $z^+ = 50$; and (c) the outer region $z/\delta_{ref} = 0.5$. There is little difference between the u and ρu -spectra, other than that the latter appear to be shifted to slightly higher frequencies. All spectra are broadband, and the broadband bump shifts to lower frequencies as the wall is approached due to the reduction in local convection speed through the boundary layer. The spectra show that some small energy is still present at the rescaling frequency and at lower frequencies. It is possible that these frequencies could be forced by the rescaling. The present data appears to indicate that such a forcing effect is probably weak, but longer time histories and better resolved spectra are required to fully assess this question.

IV. Conclusions

We have presented initial results for the DNS of a spatially-developing hypersonic turbulent boundary layer at Mach 7.2 and $Re_\theta = 1650 - 3300$. A long computational box is used with a large rescaling length to minimize spurious numerical correlation between the inflow and recycling plane. A significant initial portion of the computational box is affected by the recovery of the boundary layer from the rescaling and must be discarded. In the second part of the box, relatively good agreement with the VDII prediction is observed and the van Driest transformed velocity profile follows the log law but with a slightly different additive constant. The slight discrepancies are attributed to the wall temperature condition in the DNS.

Acknowledgments

This work was supported by the Air Force Office of Scientific Research under grant number AF 9550-09-1-0464.

References

- ¹Roy, C. J. and Blottner, F. G., “Review and assessment of turbulence models for hypersonic flows,” *Progress in Aerospace Sciences*, Vol. 42, 2006.
- ²Schrijer, F. F. J., Scarano, F., and van Oudheusden, B. W., “Application of PIV in a Mach 7 double-ramp flow,” *Experiments in Fluids*, Vol. 41, No. 2, 2006, pp. 353–363.
- ³Sahoo, D., Ringuette, M. J., and Smits, A. J., “Experimental investigation of a hypersonic turbulent boundary layer,” *AIAA*, 2009, paper 2009-780.
- ⁴Schreyer, A.-M., Sahoo, D., and Smits, A. J., “Experimental investigations of a hypersonic shock turbulent boundary layer interaction,” *AIAA*, 2011, paper 2011-481.
- ⁵Martín, M., “Direct numerical simulation of hypersonic turbulent boundary layers. Part 1. Initialization and comparison with experiments,” *Journal of Fluid Mechanics*, Vol. 570, 2007, pp. 347–364.
- ⁶Duan, L., Beekman, I., and Martín, M. P., “Direct numerical simulation of hypersonic turbulent boundary layers. Part 2. Effect of wall temperature,” *Journal of Fluid Mechanics*, Vol. 655, 2010, pp. 419–445.
- ⁷Duan, L., Beekman, I., and Martín, M. P., “Direct Numerical Simulation of Hypersonic Turbulent Boundary Layers. Part III: Effect of Mach Number,” *Journal of Fluid Mechanics*, Vol. 672, 2011, pp. 245–267.
- ⁸Duan, L. and Martín, M. P., “Direct Numerical Simulation of Hypersonic Turbulent Boundary Layers. Part IV: Effect of High Enthalpy,” *Journal of Fluid Mechanics*, 2011, accepted for publication.
- ⁹Keyes, F. G., “A summary of viscosity and heat-conduction data for He , A , H_2 , O_2 , N_2 , CO , CO_2 , H_2O , and air,” *Transactions of the American Society of Mechanical Engineers*, Vol. 73, No. 7, 1951, pp. 589–596.
- ¹⁰Jiang, G.-S. and Shu, C.-W., “Efficient implementation of weighted ENO schemes,” *Journal of Computational Physics*, Vol. 126, No. 1, 1996, pp. 202–228.
- ¹¹Martín, M., Taylor, E., Wu, M., and Weirs, V., “A bandwidth-optimized WENO scheme for the effective direct numerical simulation of compressible turbulence,” *Journal of Computational Physics*, Vol. 220, No. 1, 2006, pp. 270–289.
- ¹²Williamson, J. H., “Low-storage Runge–Kutta schemes,” *Journal of Computational Physics*, Vol. 35, No. 1, 1980, pp. 48–56.

¹³Xu, S. and Martín, M., “Assessment of inflow boundary conditions for compressible turbulent boundary layers,” *Physics of Fluids*, Vol. 16, No. 7, 2004, pp. 2623–2639.

¹⁴van Driest, E. R., “The problem of aerodynamic heating,” *Aeronautical Engineering Review*, Vol. 15, No. 10, 1956, pp. 26–41.

¹⁵Hopkins, E. J. and Inouye, M., “An evaluation of theories for predicting turbulent skin friction and heat transfer on flat plates at supersonic and hypersonic Mach numbers,” *AIAA Journal*, Vol. 9, No. 6, 1971, pp. 993–1003.

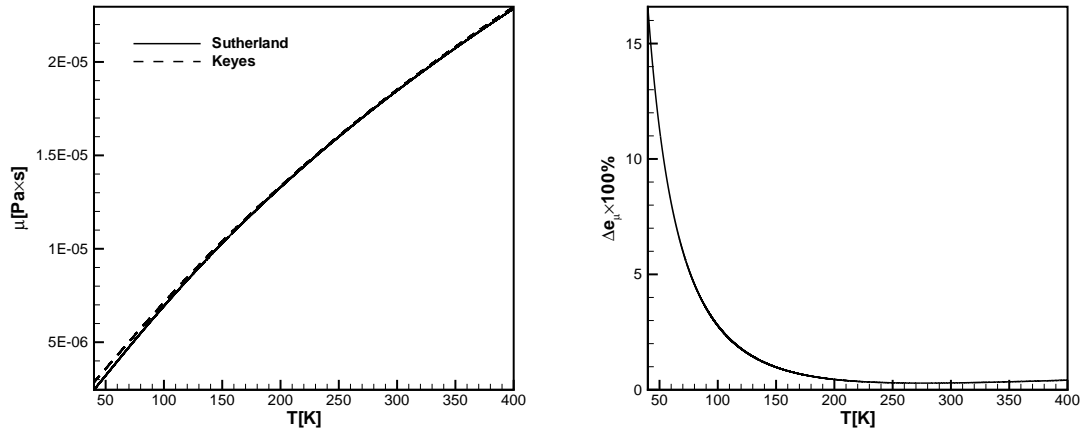


Figure 1. Comparison of Sutherland's and Keyes viscosity model for the range of temperatures present in the DNS.

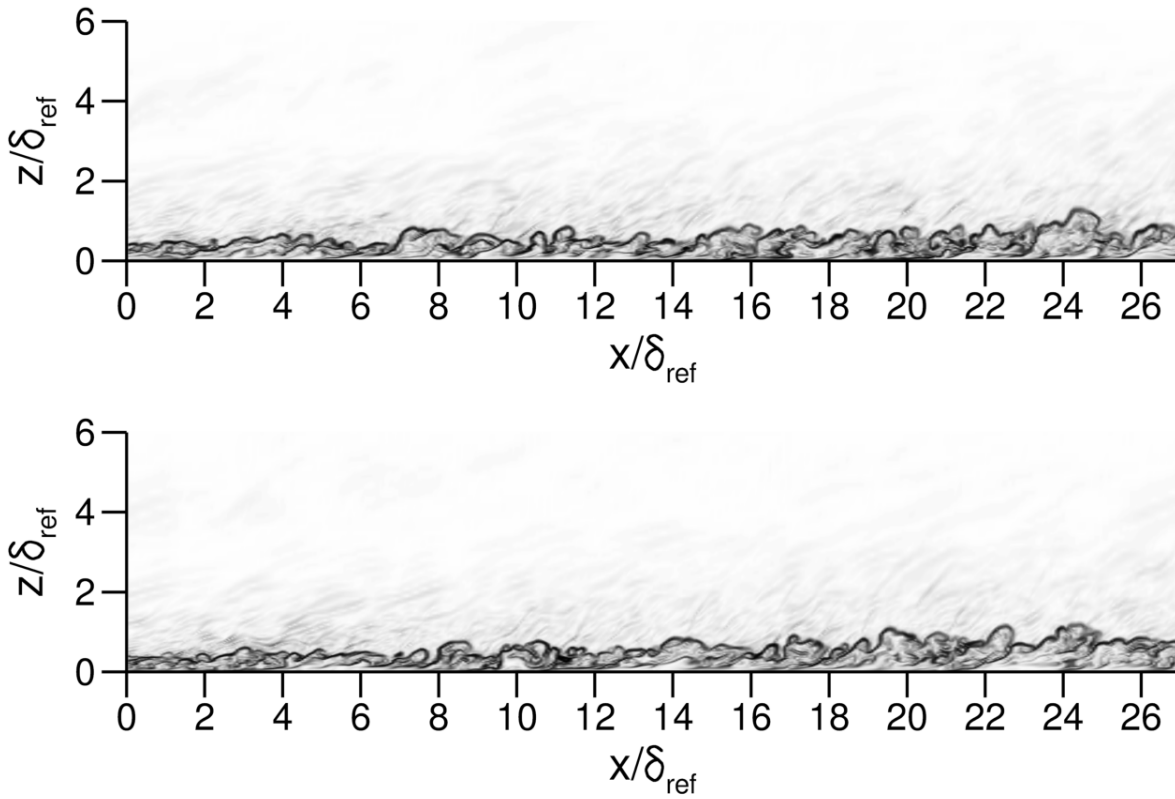


Figure 2. Typical instantaneous flow visualizations (uncorrelated). Gray-scale contour map of $\exp(-0.25|\nabla\rho|)$ (numerical Schlieren).

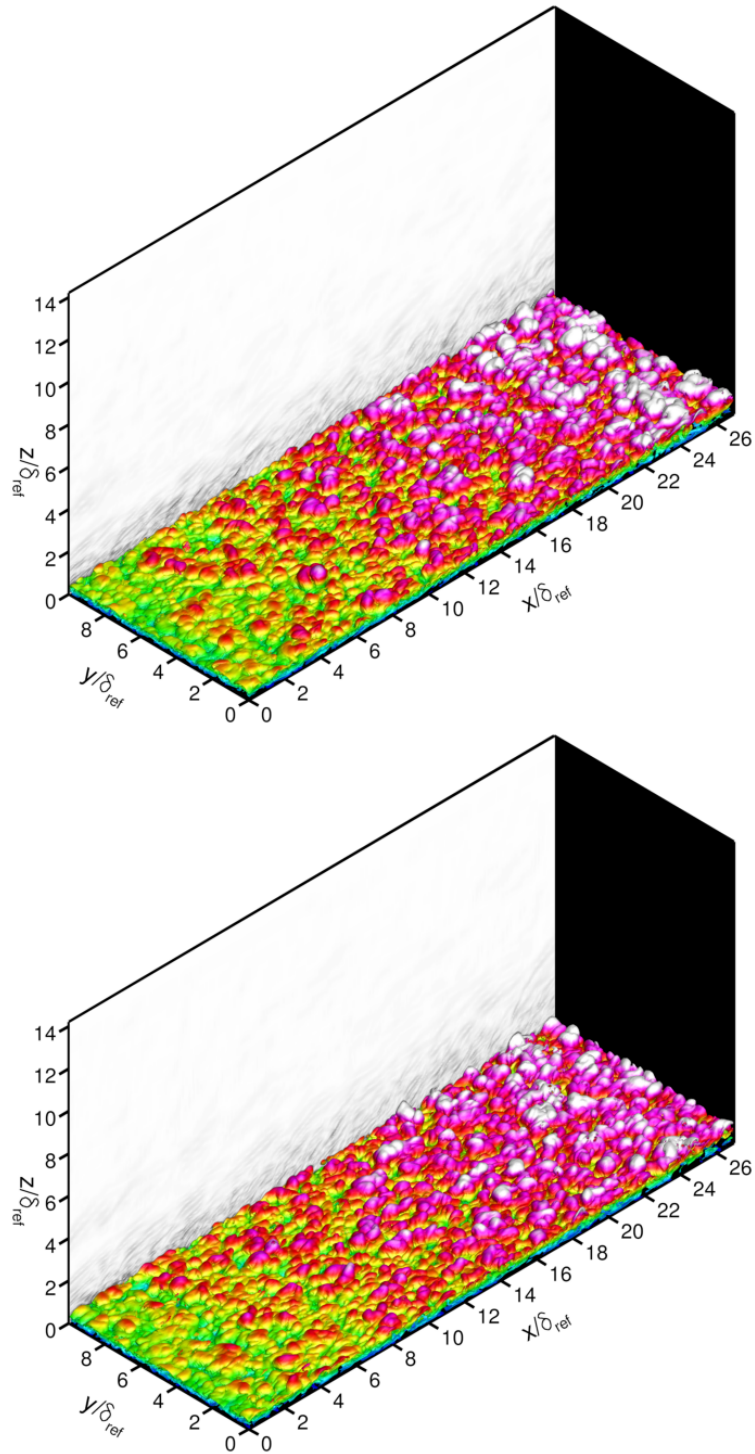


Figure 3. Typical instantaneous flow visualizations (uncorrelated). Isosurface of magnitude of density gradient $|\nabla\rho|\delta_{ref}/\rho_\infty = 3.0$ colored by the wall normal coordinate z . The color map goes from blue (corresponding to the wall) to white (corresponding to $z/\delta_{ref} = 1$). A gray-scale contour map of $\exp(-0.5|\nabla\rho|)$ is shown on the (x, z) -plane at the $y = L_y$ -boundary of the domain.

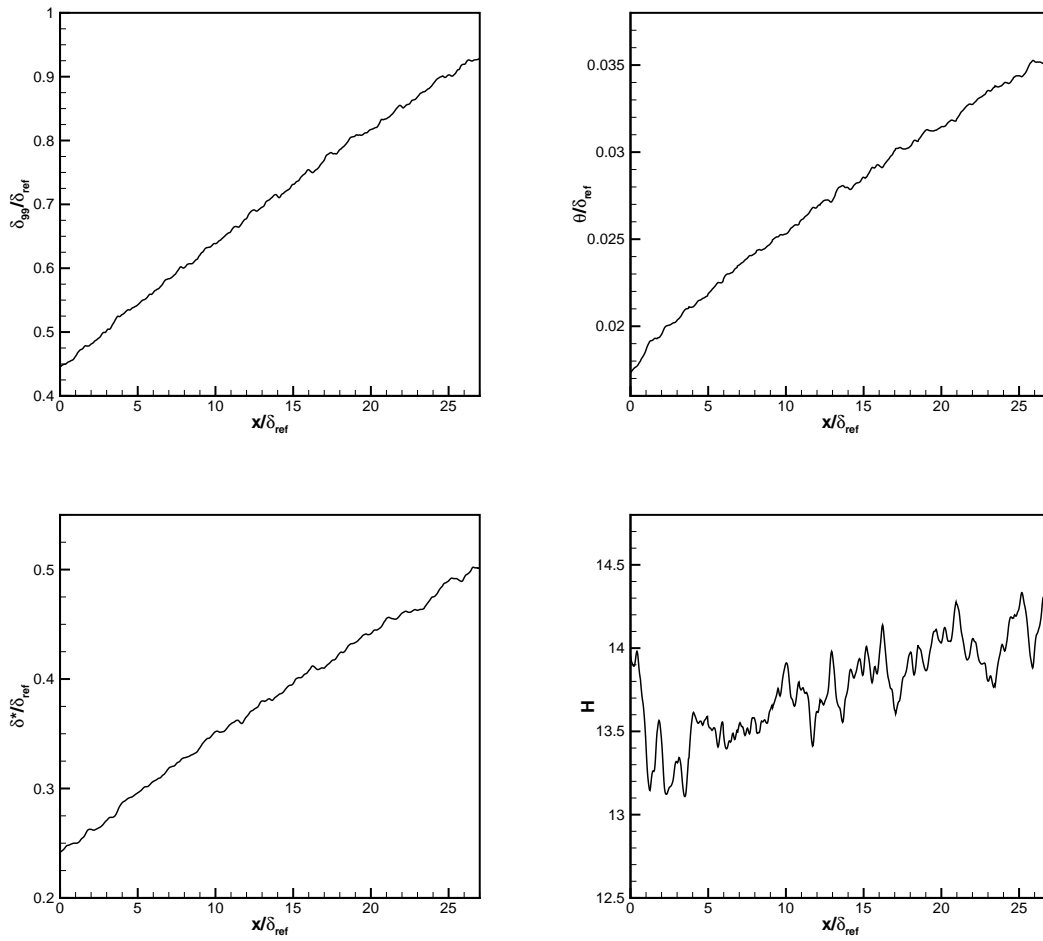


Figure 4. Evolution of boundary layer parameters δ_{99} , θ , δ^* and H with streamwise distance.

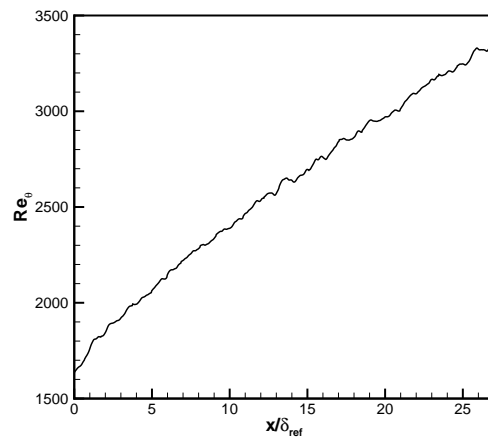


Figure 5. Evolution of Reynolds number based on momentum thickness Re_θ with streamwise distance.

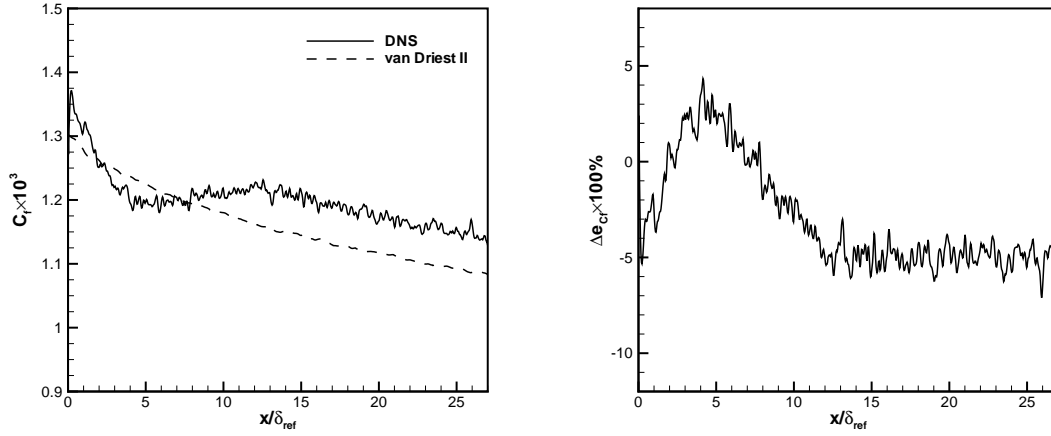


Figure 6. Evolution of skin friction coefficient C_f and of $\Delta e_{Cf} = (C_{f,VDII} - C_f)/C_f$ with streamwise distance.

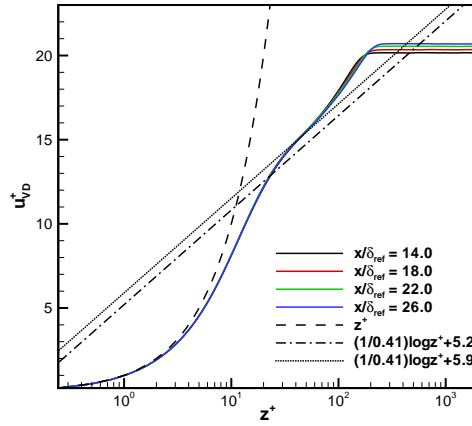


Figure 7. van Driest transformed velocity u_{vD}^+ at different streamwise locations.

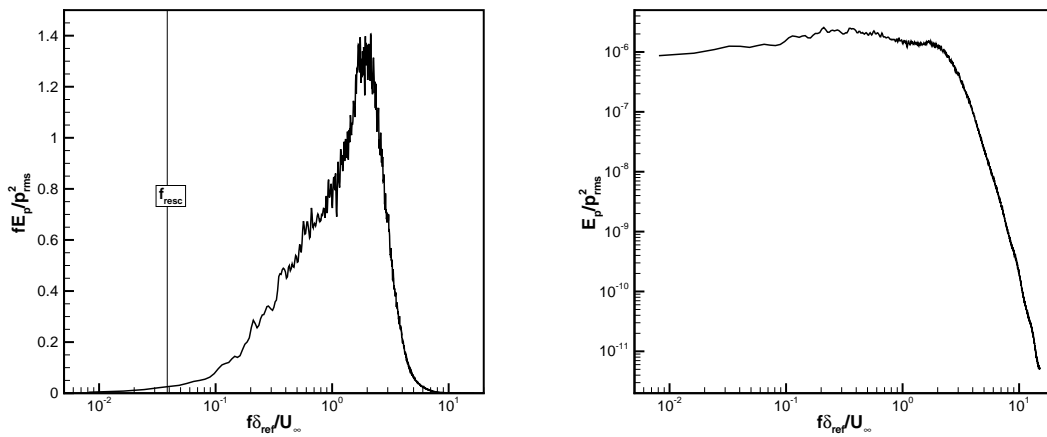


Figure 8. Spectrum of wall pressure at the recycling location $x_{rec}/\delta_{ref} = 26.0$.

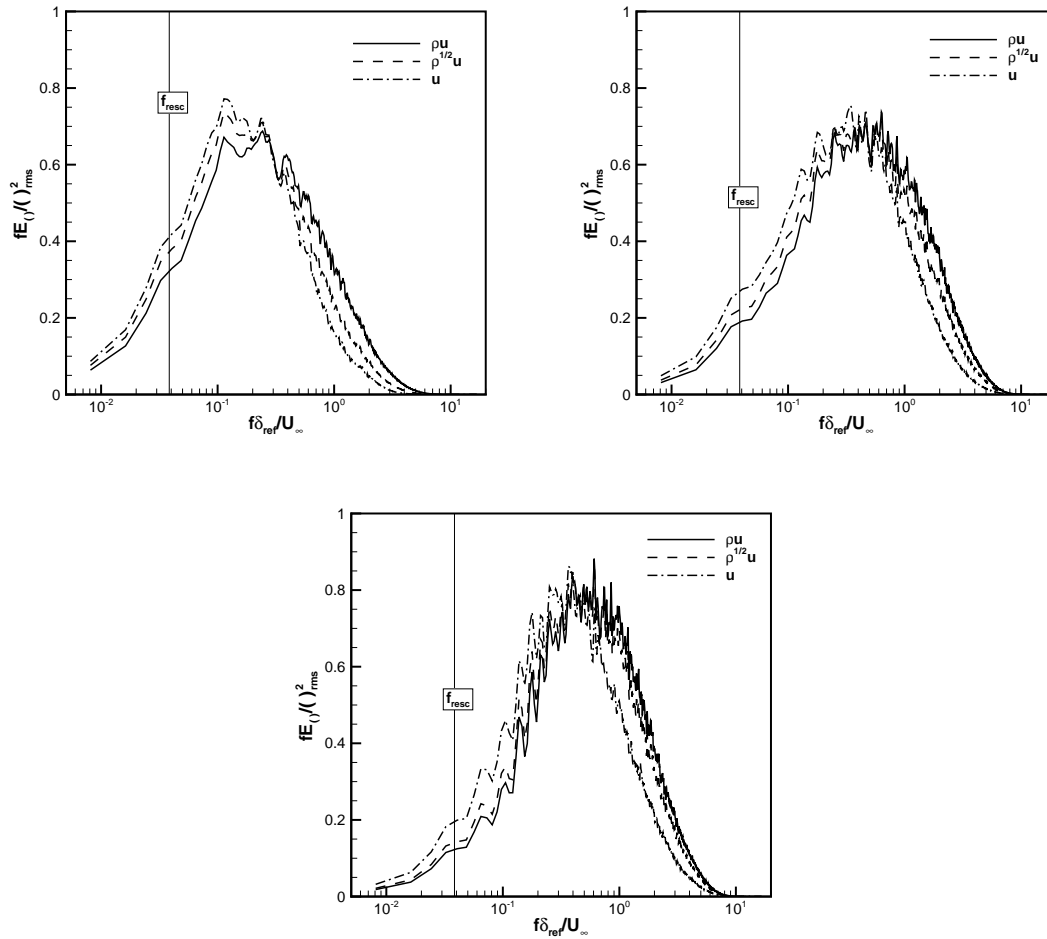


Figure 9. Spectra at the recycling location $x_{rec}/\delta_{ref} = 26.0$ and at three wall normal locations: $z^+ = 15$, $z^+ = 50$ and $z/\delta_{ref} = 0.5$.